Supplementary Information (SI) for Green Chemistry.
This journal is © The Royal Society of Chemistry 2026

Supplementary Information

A green versatile platform for synthesising renewable ether-based thermoplastic elastomers

Sungkwon Yoon[a], Charlie Bateman[a,b], James J. C. Busfield[c], Peter J. Martin[a], and Biqiong Chen*[,a,b]

[a]School of Mechanical and Aerospace Engineering, Queen's University Belfast, Stranmillis Road, Belfast, BT9 5AH, United Kingdom

[b]Department of Chemistry, University of Liverpool, Crown Street, Liverpool, L69 7ZD, United Kingdom

[c]School of Engineering and Materials Science, Queen Mary University of London, Mile End Road, London, E1 4NS, United Kingdom

*Corresponding author. Email address: biqiong.chen@liverpool.ac.uk

Characterisation

For distortionless enhancement by polarisation transfer (DEPT) ^{13}C nuclear magnetic resonance (NMR) spectroscopy, a resonance frequency of 100.6 MHz was used with the DEPT135 carbon-13 method and a 30° excitation pulse program of zg30 pulse sequence (256 scans, 16 – 32 ppm spectral width, 4 s recycle delay).

X-ray diffraction (XRD) pattern was acquired by a Malvern Panalytical X'Pert Pro Multi-Purpose X-ray Diffractometer (Cu $K_{\alpha 1}$; λ = 0.15406 nm; 45 kV; 40 mA; scan range: 5 – 65°; scan rate: 0.1° s^{-1}). Elastomer samples were cryo-milled using Rondol 6850 cryogenic mill to obtain fine powder prior to the test.

Ultraviolet–visible (UV-vis) spectroscopy was performed on an Agilent Cary 60 using solid elastomer specimens with a thickness of 2.01 – 2.04 mm. Spectra were calibrated by 0 and 100% absorption baselines at a resolution of 1 nm.

The chemical stability was studied according to ISO 175. The disk specimens of each TPU were prepared by punching (diameter: 5.94 – 5.99 mm, thickness: 1.92 – 2.03 mm, n = 3) and dried in a vacuum oven at 40 °C for 2 days until a constant weight was acquired. The specimens were then completely submerged in the following liquids in sealed test tubes: distilled water (pH = 6.8), hydrochloric acid solution (pH = 3.8) and sodium hydroxide solution (pH = 9.8), acetone, ethanol and mineral oil. These three pH values were selected based on the pH values for neutral water, acidic rains[72] and the pH ranges of household detergents, sea water and concrete pore water samples[73,74]. They are commonly used to test the stability or degradation of polymers[75-77]. At day 1 and 7, samples were removed from the liquids, dried by blotting with filter paper, and weighed using a four-decimal scale (Sartorious M-power). The test liquids were shaken once a day and replaced with fresh ones weekly following the standard. The test result was reported gravimetrically following equation (S1), where m_{ini} and m_{day} are

the initial weight before testing and the weight measured at the specific incubation day, respectively, using the analytical scale.

$$Weight\ change = \frac{m_{day} - m_{ini}}{m_{ini}} \times 100\ (\%) \#(S1)$$

Density (ρ) was measured from rectangular specimens at ambient laboratory temperature (20 ± 2 °C). The specimens were dried in a vacuum oven at 40 °C for 24 h prior to the measurement. Specimen weights (m) were measured on the analytical scale. Dimensions: length (l), with (w) and thickness (t), were measured by a digital calliper with a 0.01 mm resolution (Mitutoyo CD-P15P) to calculate volume ($V = l \times w \times t$). The density was calculated by equation (S2).

$$\rho = \frac{m}{V}\ (g\ cm^{-3}) \#(S2)$$

The melt flow index (MFI) measurements were done, following ASTM D1238 using a Kayeness Galaxy Model 7053, at 160 °C with a melting time of 7 min and a load of 2.16 kg. At the time interval of 30 s, 3 cuts were made from the exudate through the die orifice. The cuts were allowed to cool down to ambient laboratory temperature (20 ± 2 °C) and weighed. The factor of 20 was multiplied to acquire MFI according to the standard.

Colouring tests were performed with curcumin and solvent green 3 dyes. The dyes were mixed with the TPU (LHH) elastomer powders by mechanical agitation at 300 rpm for 3 h and hot pressed in a circle frame at 160 °C for 10 min. To observe fluorescent behaviour of curcumin-dyed sample, an Analytik Jena High-Intensity, long-wave UV lamp (B-100AP) with an exposure box was used.

Determination of hydroxyl numbers by titration

The hydroxyl number of the long-chain polyether diols was determined by phthalation followed by colourimetric titration, according to ISO 14900. The synthesised polyether diols were dissolved in pyridine and underwent phthalation by phthalic anhydride with presence of imidazole catalyst in round bottom flasks. Each flask was connected to a reflux condenser. A blank test was also performed to normalise the results. After hydrolysation of excess anhydride by water, the resulting phthalic acid was titrated by NaOH solution (0.5 N). The colourimetric titration end point was determined when the first faint pink from the phenolphthalein indicator appeared and lasted for more than 15 sec. The hydroxyl number was determined by equation (S3).

$$Hydroxyl\ number = \frac{(V_b - V_s \times 0.5 \times 56.1)}{m} \#(S3)$$

where V_b is the volume of NaOH solution required for titration of the test samples. V_s is the volume of the NaOH solution required for titration of the blank. 0.5 is the concentration of the titrant, NaOH solution. 56.1 is the molecular weight of NaOH, and m is the sample weight. The test was triplicated.

The measured hydroxyl values from the polyether diols from each synthesis time resulted in 33.9 mg KOH g^{-1} for 7 h of the synthesis time (from a batch with $\bar{M}_n$ of 2000 g mol^{-1}) and 13.7 mg KOH g^{-1} for 19 h (from a batch with $\bar{M}_n$ of 4900 g mol^{-1}). These values are lower than their theoretical hydroxyl numbers of 56.1 mg KOH g^{-1} (1.00 mmol of hydroxyl end groups per gram for $\bar{M}_n$ of 2000 g mol^{-1}) and 23.0 mg KOH g^{-1} (0.41 mmol of hydroxyl end groups per gram for $\bar{M}_n$ of 4900 g mol^{-1}). This implies that the branched molecular structure in the polyether diols, inherited from their building blocks of Pripol 2030, exerted steric hindrance to the hydroxyl end groups to react.[78]

Nomenclature of renewable ether-based thermoplastic elastomers

Sample codes of thermoplastic polyurethane (TPU) elastomers are presented as XYZ in this study, where X represents S for the short (7 h) or L for the long (19 h) synthesis time of the used polyether diols. Y stands for the chosen diisocyanate species in the hard segment: I for IPDI, M for MDI and H for HMDI. Z tells the hard segment molar ratio: L for low, M for medium and H for high ratios. For instance, the sample coded SML was synthesised with the polyether diol with the short synthesis time of 7 h, MDI in the hard segment, and a relatively low molar ratio of the hard segment molar ratio amongst the TPU compositions studied in this work.

Polyurethane urea is abbreviated into PUU. Sample codes of thermoplastic polyether-ester (TPEE) elastomers are presented as EEL and EEH. EEL has the lower hard segment molar ratio of 1:0.28:1.16 (polyether diol:BDO:DMT), whereas EEH has the higher hard segment molar ratio of 1:3.9:5.4 (polyether diol:BDO:DMT).

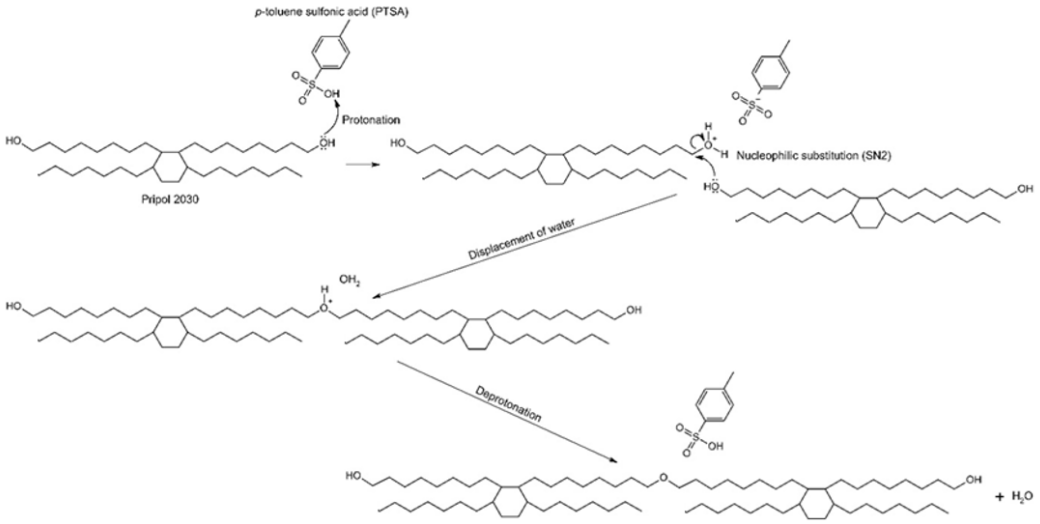

Fig. S1: Chemical scheme showing S_N2 reaction mechanism in the formation of ether linkages between Pripol 2030 for the production of biobased long-chain polyether diols with PTSA catalyst.

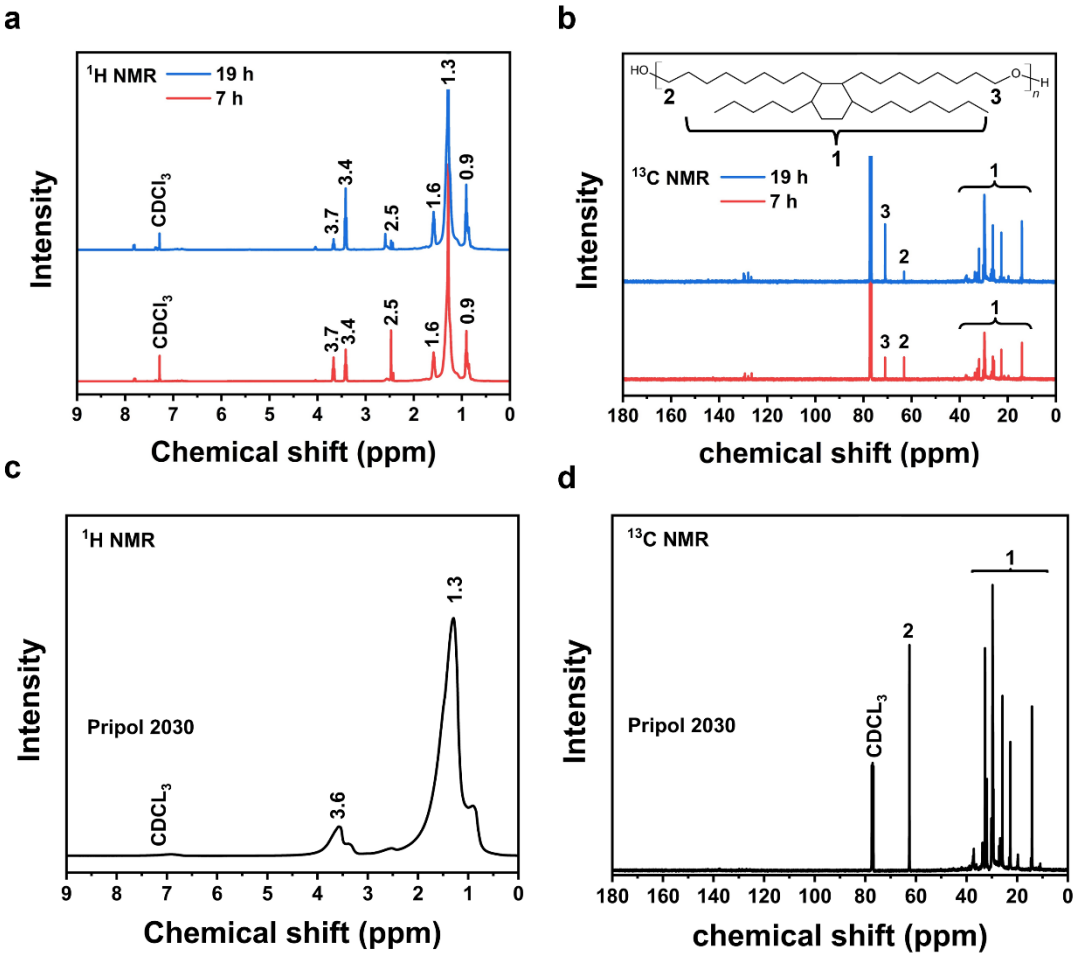

Fig. S2: a, ^{1}H and b, ^{13}C NMR spectra of the biobased long-chain polyether diols with the synthesis time of 7 and 19 h. c, ^{1}H and d, ^{13}C NMR spectra of Pripol 2030. Spectra were shifted vertically for visual clarity.

Notes: ^{1}H NMR spectra show the methylene (CH_2) proton adjacent to the terminal hydroxyl end groups (CH_2–OH) appears at 3.7 ppm for the polyether diols and 3.6 ppm for Pripol 2030.[15] The CH_2 proton bonded with ether linkages (C–O–C) appears at 3.4 ppm in the polyether diols. The terminal hydroxyl (OH) end group proton appears at 2.5 ppm which decreased in the sample with a synthesis time from 7 to 19 h, suggesting more OH groups have been consumed with increasing reaction time. The peaks at 0.9, 1.3 and 1.9 ppm corresponds to the methyl (CH_3) proton at the end of the branched alkyl chains, the CH_2 proton and mid-chain CH proton, respectively.[16] Small peaks at 4.0 ppm are present for the CH_2 proton near carbon double bond

(C=C) from imperfect hydrogenation of fatty acids in Pripol 2030 and the aromatic structures in the PTSA catalyst and in some cases also Pripol 2030.[79,80] From the integral values for the protons in the CH_2–OH for the Pripol 2030 and the two polyether diols, it was calculated that their extents of reaction were 75.5% and 90.7% for the 7 h and 19 h, respectively. The longer reaction time led to a higher extent of reactions.

^{13}C NMR spectra show deshielded carbon at C–O–C and shielded terminal carbon at CH_2–OH appear at 71 and 63 ppm, respectively.[16] The longer synthesis time of 19 h exhibits an increase in the intensity corresponds to the C–O–C and a decrease in the terminal OH carbon, indicating formation of more ether linkages by consuming more terminal hydroxyl groups. The peaks below 40 ppm can be assigned to the carbons in the main backbone structure, with the terminal CH_3 on the branched alkyl chains and mid-chain CH_2 at 14 and 30 ppm, respectively.[15] Minor C=C peaks are also seen at around 129 ppm. The spectra were shifted vertically for visual clarity.

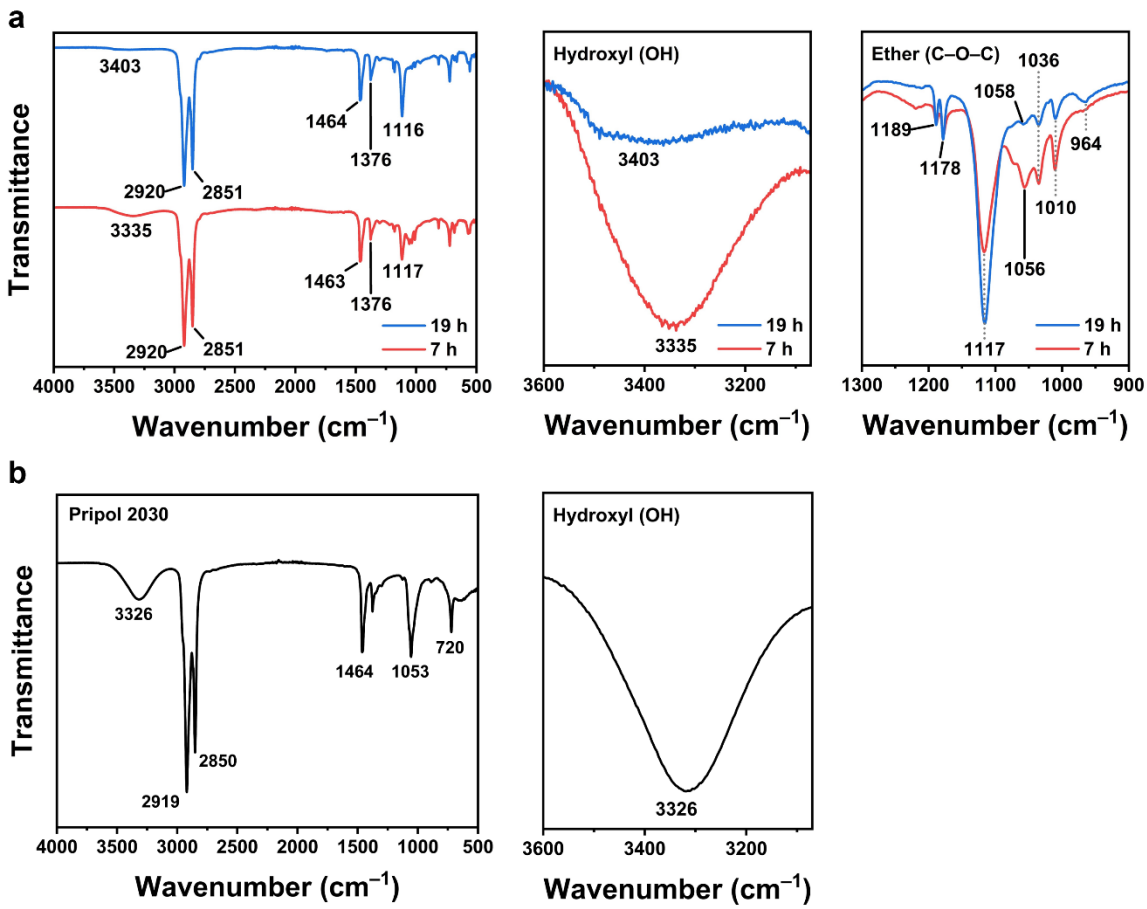

Fig. S3: FTIR spectra of a, biobased long-chain polyether diols and b, Pripol 2030. Spectra were shifted vertically for visual clarity.

Notes: With increasing synthesis time, the OH peak greatly reduces its intensity and shifts from 3326 cm^{-1} for Pripol 2030 to higher wavenumbers, 3335 cm^{-1} for 7 h and 3403 cm^{-1}. Increasing synthesis time also enhances the intensity of asymmetric C–O–C stretching vibration peak at 1117 cm^{-1}.[15,81] The peaks between 1060 and 1000 cm^{-1}, which correspond to the OH end groups, also decrease, indicating more ether linkage formation.[82] The peaks at 2920, 2851, 1178 and 964 cm^{-1} (stretching and twisting vibration of CH_2) as well as 1464 or 1463 and 1376 cm^{-1} (bending vibration of CH_3) can be assigned to the main carbon backbone chain structures.[83]

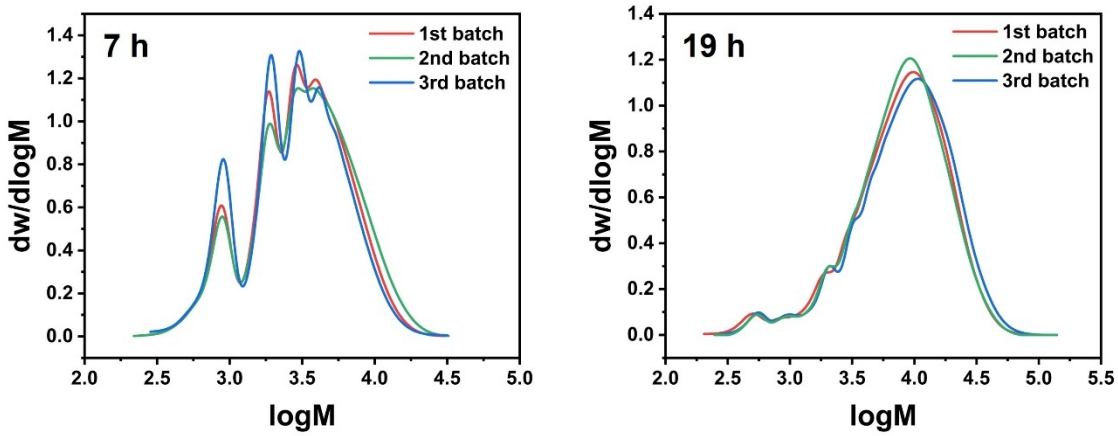

Fig. S4: GPC traces of biobased polyether diols with the synthesis time of 7 h and 19 h.

Notes: Three repeats for each synthesis time are presented here, demonstrating the reproducibility of the synthesis of the polyether diols. The number average molecular weights, $\bar{M}_n$, of polyether diols, are 2200 ± 100 g mol^{-1} for 7 h to 4700 ± 200 g mol^{-1} for 19 h, respectively. For the 7 h, the first peak (15%) shows an average peak molecular weight, $\bar{M}_p$, of 891 g mol^{-1}, which could be attributed to the reacted product of the dimmer alcohol with the minor monomeric alcohol, as well as the unreacted minor trimer alcohol. The three shoulders in the main peak are due to the presence of monomeric and trimer alcohols in the Pripol 2030 causing to non-uniform products. For the 19 h, the first peak (2.0%) shows an $\bar{M}_p$ of 525 g mol^{-1}, close to the molecular weight of unreacted dimer alcohol. The second peak (1.8%) shows an $\bar{M}_p$ of 948 g mol^{-1}, which again could be associated with the reacted product of the dimmer alcohol with the monomeric alcohol, as well as the unreacted trimer alcohol.

Table S1: The number average molecular weight ($\bar{M}_n$), weight average molecular weight ($\bar{M}_w$) and polydispersity index (PDI) of long-chain polyether diols by GPC.

Synthesis time	$\bar{M}_n$	$\bar{M}_w$	PDI
7 h	2200 ± 100	4000 ± 300	1.8 ± 0.0
19 h	4700 ± 200	11000 ± 500	2.3 ± 0.1

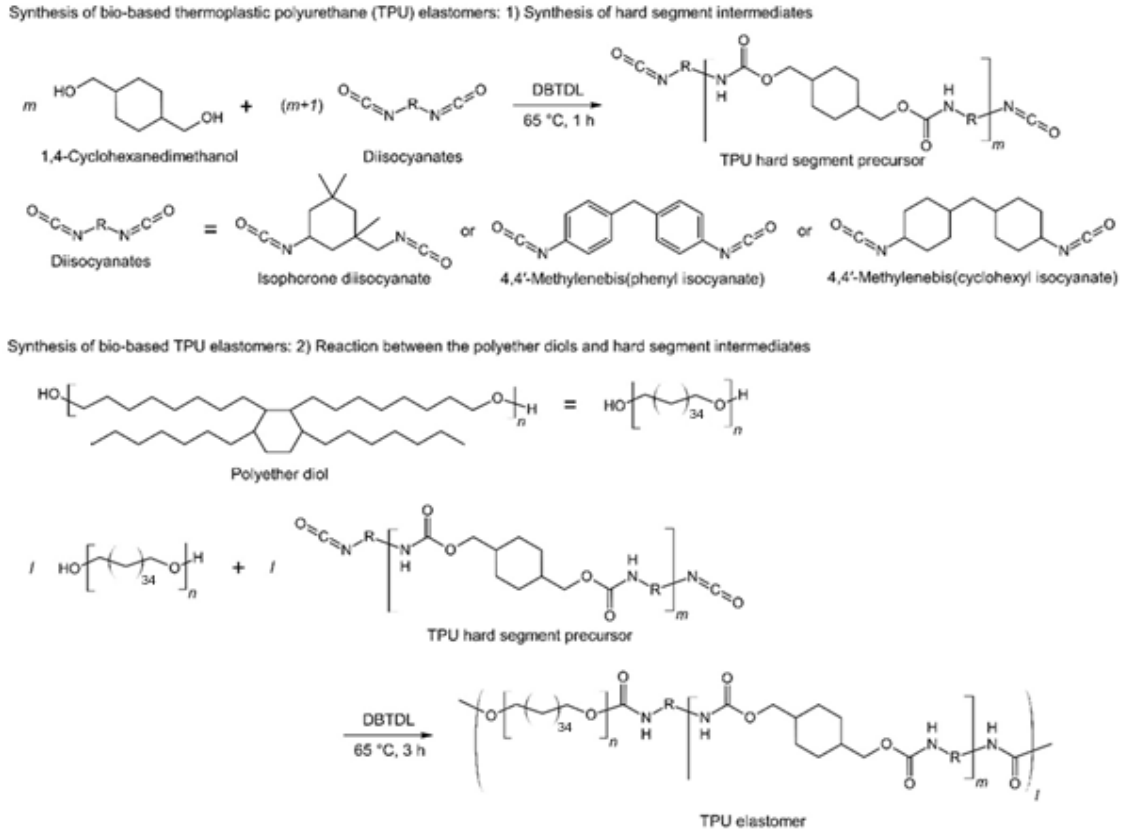

Fig. S5: Chemical scheme showing the synthesis of ether-based TPU elastomers.

Table S2: Summary of ether-based TPU formulations.

Polyether diol synthesis time / h	Hard segment		Molar ratio (Polyether diol:chain extender: diisocyanate)	Hard segment content / % w/w	Soft segment content / % w/w	Sample code[a]
	Chain extender	Diisocyanate or DMT				
7	CHDM	IPDI	1:2.50:4.31	37.7	62.3	SIL
7	CHDM	IPDI	1:3.33:5.17	42.8	57.2	SIM
7	CHDM	MDI	1:2.50:4.31	39.8	60.2	SML
7	CHDM	MDI	1:3.33:5.17	44.9	55.1	SMM
7	CHDM	HMDI	1:2.50:4.31	40.7	59.3	SHL
7	CHDM	HMDI	1:3.33:5.17	45.8	54.2	SHM
19	CHDM	IPDI	1:3.33:5.17	25.6	74.4	LIM
19	CHDM	IPDI	1:4.17:6.03	29.0	71.0	LIH
19	CHDM	MDI	1:3.33:5.17	27.2	72.8	LMM
19	CHDM	MDI	1:4.17:6.03	29.0	71.0	LMH
19	CHDM	HMDI	1:3.33:5.17	27.9	72.1	LHM
19	CHDM	HMDI	1:4.17:6.03	31.5	68.5	LHH

[a]molar ratio of hard segment (chain extender + diisocyanate) to soft segment of 6.81 is considered low L; 8.50 medium M; and 10.20 high H in the sample codes.

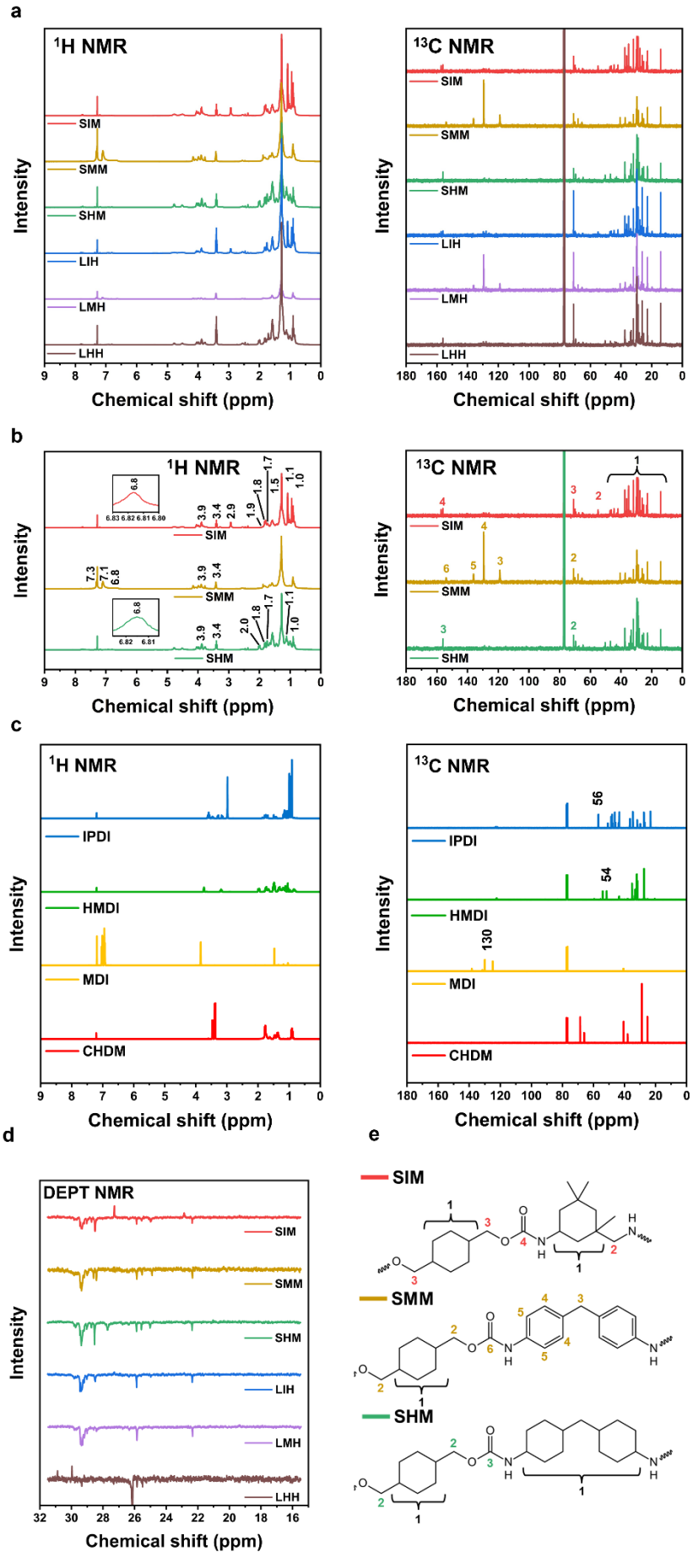
a
^{1}H NMR
SIM
SMM
SHM
LIH
LMH
LHH
Intensity
Chemical shift (ppm)
^{13}C NMR
b
c
IPDI
HMDI
MDI
CHDM
56
54
130
d
DEPT NMR
e

Fig. S6: ^{1}H and ^{13}C NMR spectra of ether-based TPU elastomers. a, NMR spectra of TPUs. The spectra were shifted vertically for visual clarity. **b**, NMR spectra showing the regions of interest. The peak annotation in the ^{13}C NMR spectra corresponds to the annotated carbon in Fig. S6e. **c**, NMR spectra for the starting components of TPU hard segments. **d**, DEPT NMR spectra of TPUs. The spectra have been shifted for visual clarity. **e**, The hard segment chemical structure of TPU with annotated carbons with the corresponding peaks in ^{13}C NMR spectra (Fig. S6b).

Notes: Under ^{1}H NMR, SMM TPU elastomers with aromatic MDI component show aromatic proton peaks at 7.1 and 7.3 ppm.[21] All TPUs (SIM, SMM and SHM) exhibit a peak at 6.8 ppm which can be correlated with the N–H proton in the urethane linkages.[21] Cycloaliphatic and aliphatic group protons are shown between 1.0 and 2.0 ppm for SIM and SHM by containing IPDI or HMDI.[15] SIM shows a distinct IPDI methylene proton peak at 2.9 ppm.[21,22] The CH_2–O protons are shown at 3.4 and 3.9 ppm. Under ^{13}C NMR, the peak at 154 ppm or 156 ppm is related to the carbonyl (C=O) group in the urethane linkages. SMM shows aromatic ring carbons at 136 ppm and 129 ppm, shifted from 130 ppm in MDI, with the additional methylene carbon at 119 ppm.[84] The peak at 71 ppm is attributed to the O-bonded carbon (O–CH_2).[21,84] SIM shows the N-bonded carbon (N–CH_2) at 55 ppm, shifted slightly from 56 ppm in IPDI.[85] The peaks under 40 ppm are correlated with the carbon backbone structure of the elastomers and DEPT NMR analysis in Fig. S6d differentiates between the carbon structures with CH_2 groups appearing in the negative direction and CH groups appearing in the positive direction.[21,84]

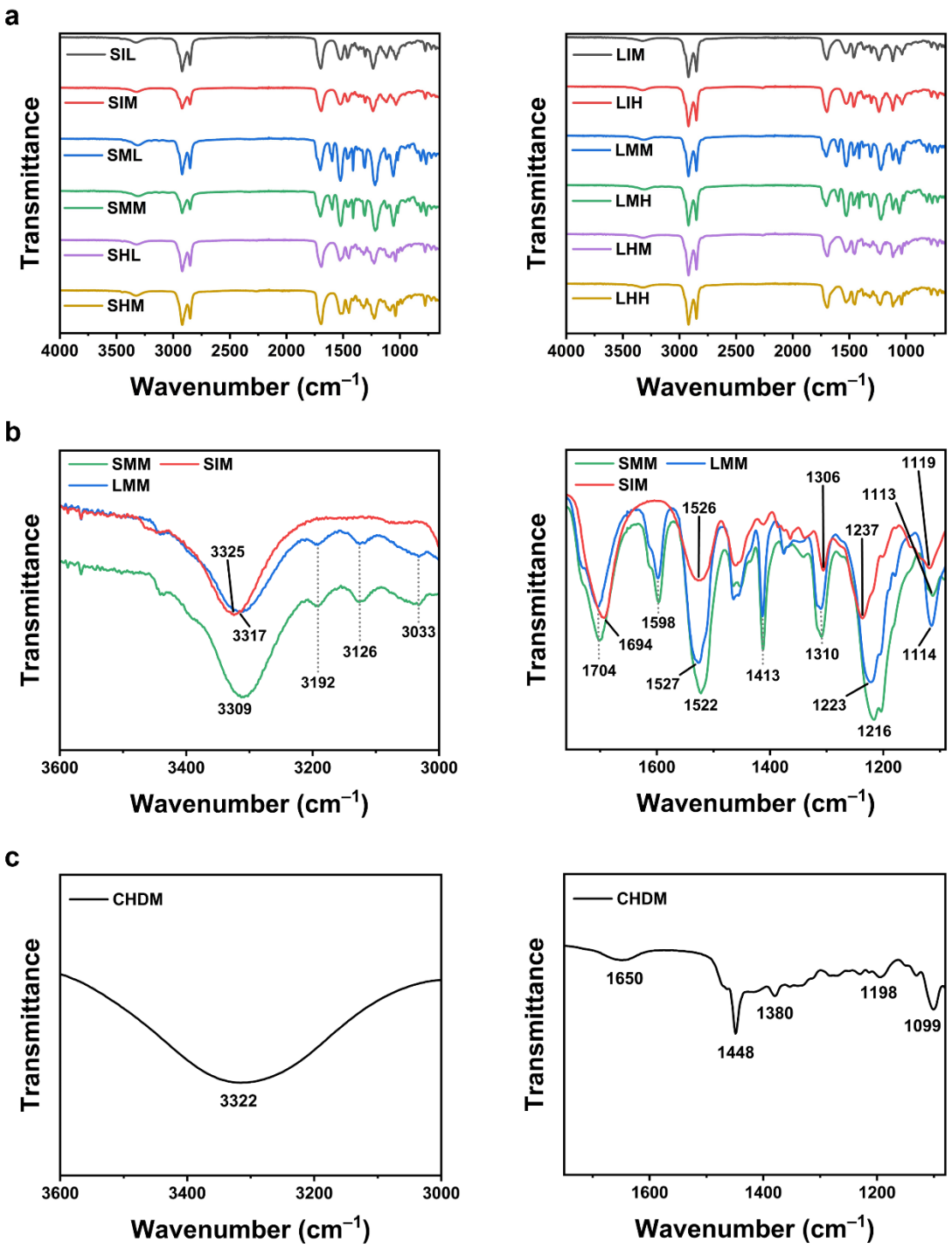

Fig. S7: FTIR Spectra of ether-based TPU elastomers. a, FTIR spectra of TPUs. The spectra were shifted vertically for visual clarity. b, FTIR spectra showing the regions of interest. c. FTIR spectrum of CHDM.

Notes: SMM and LMM TPU show the broad peak from 3325 to 3309 cm^{-1} which can be attributed to N–H stretching of amide A.[15] The O-H peak of CHDM appears at a similar

position at 3322 cm^{-1}. Between SMM and LMM, the amide A peak shifts to a lower wavenumber in SMM which indicates stronger hydrogen bonding with this functional group, mainly due to its higher hard segment ratio than LMM. Peaks related to the urethane linkages are shown at 1704 – 1694 cm^{-1} (C=O stretching band, free or amide I), 1526 – 1522 cm^{-1} (N–H bending of amide II), 1310 – 1306 cm^{-1} (C–N stretching vibration), 1237 – 1216 cm^{-1} (N–H bending of amide III) and 1119 – 1114 cm^{-1} (O–C–C stretching vibration).[15,24,25] The red shift and enhanced peak intensity of N–H peaks in SMM compared to SIM suggests the formation of a higher degree of hydrogen bonding and subsequent increase in phase separation in SMM by denser chain packing on the hard segment.[86,87] SMM and LMM show the aromatic hard segment structure by the three peaks in the range of 3192 – 3033 cm^{-1} (=C–H stretching vibration), 1598 cm^{-1} (aromatic C=C stretching) and 1413 cm^{-1} (aromatic C–H in plane vibration).[87,88]

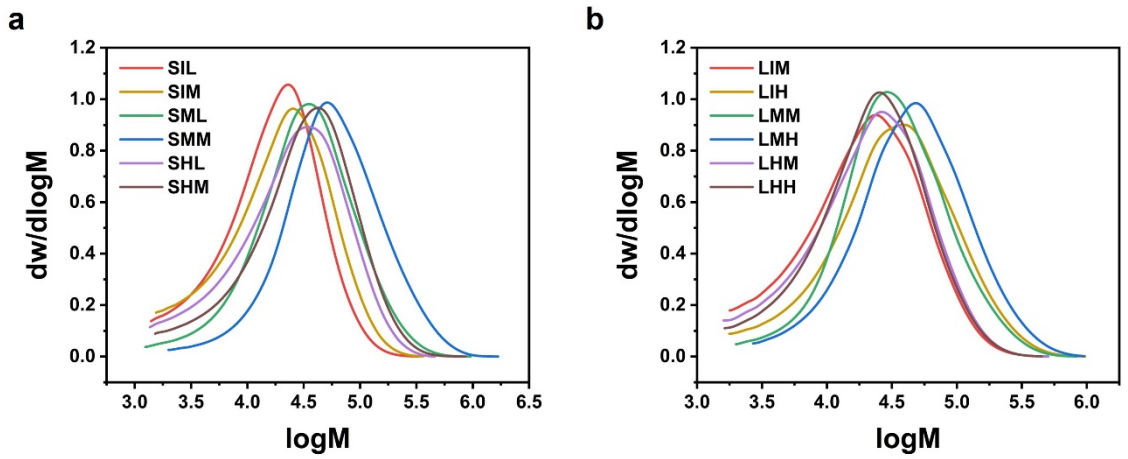

Fig. S8: GPC traces of ether-based TPU elastomers from the **a**, short polyether diol and **b**, long polyether diol.

Table S3: $\bar{M}_n$, $\bar{M}_w$ and PDI of ether-based TPU elastomers by GPC.

Sample code	$\bar{M}_n$	$\bar{M}_w$	PDI
SIL	10100	24500	2.42
SIM	11000	30100	2.73
SML	17800	50800	2.85
SMM	32200	90000	2.79
SHL	12500	39800	3.18
SHM	16200	48700	3.00
LIM	11600	30400	2.62
LIH	17500	54000	3.08
LMM	20600	50300	2.44
LMH	27400	71200	2.59
LHM	12200	33300	2.72
LHH	13100	32900	2.51

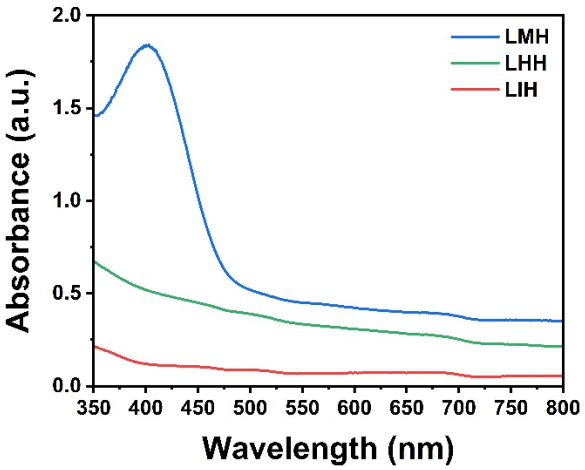

Fig. S9: UV-vis spectra of ether-based TPUs (LMH, LHH and LIH) across the visible light wavelength range.

Notes: An absorbance of 2.0 means 99% of available light is being absorbed. The transparent TPUs of LIH and LHH show minimal absorption across the measured wavelengths, while the translucent LMH shows a strong absorption peak centred at 400 nm.

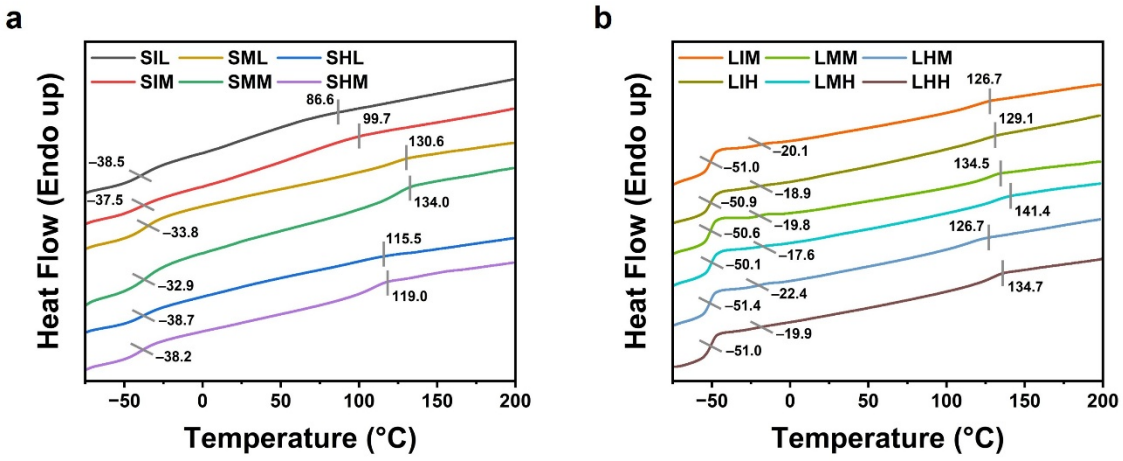

Fig. S10: DSC 2nd heating curves of ether-based TPUs from the **a**, shorter polyether diol and **b**, longer polyether diol. The curves were shifted vertically for visual clarity.

Notes: LMM TPU shows a glass transition at a lower temperature than SIM, SML and SMM TPUs with the shorter polyether diol. Between SIM, SML and SMM, the aromatic hard segment in SML and SMM leads to higher glass transition temperatures than the cycloaliphatic hard segment in SIM, as the symmetrical and aromatic molecular structure of MDI is known to form a stronger intermolecular hydrogen bonding between the hard segments.[32] Between SML and SMM, SMM shows a higher glass transition temperature due to its higher hard segment ratio than SML. Another finding is that a secondary glass transition temperature appears between –22.4 and –17.6 °C when the longer polyether diol is used in the TPU formulations, possibly caused by the surface-bound soft segment domains on the hard segment microphases, slowing down the molecular motions.[89] These "free" and "constrained" soft segment glass transitions are known to be at around –50 to –40 °C and –20 to –10 °C, respectively, [89] which align well with glass transition behaviours in our TPUs. The melting point follows a similar trend to the glass transition temperature. The increasing hard segment ratio promotes crystallisation of these hard domains forming stronger and more tightly packed structures yielding higher glass transition temperature and melting point.[90] However for LMM,

the melting point is slightly higher than SMM, even when the hard segment ratio is lower because of the use of the longer polyether diol, possibly due to the enhanced mobility of the hard segments in LMM, with the longer, amorphous and flexible polyether diol soft segments surrounding the hard segment domains.[91]

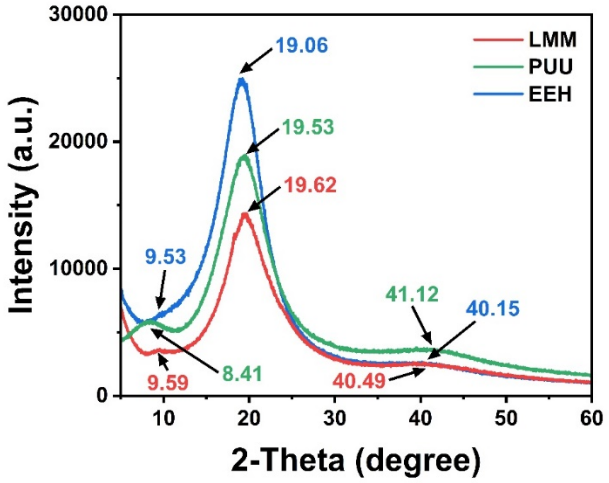

Fig. S11: XRD patterns of LMM (TPU), PUU and EEH (TPEE).

Notes: Broad diffraction peaks are seen at 2Θ around 9°, 20° and 40°, reflecting mostly amorphous polymer structures lacking a long-range ordered crystalline structure.[92] The coloured peak notations correspond to each sample: red for LMM, green for PUU and blue for EEH.

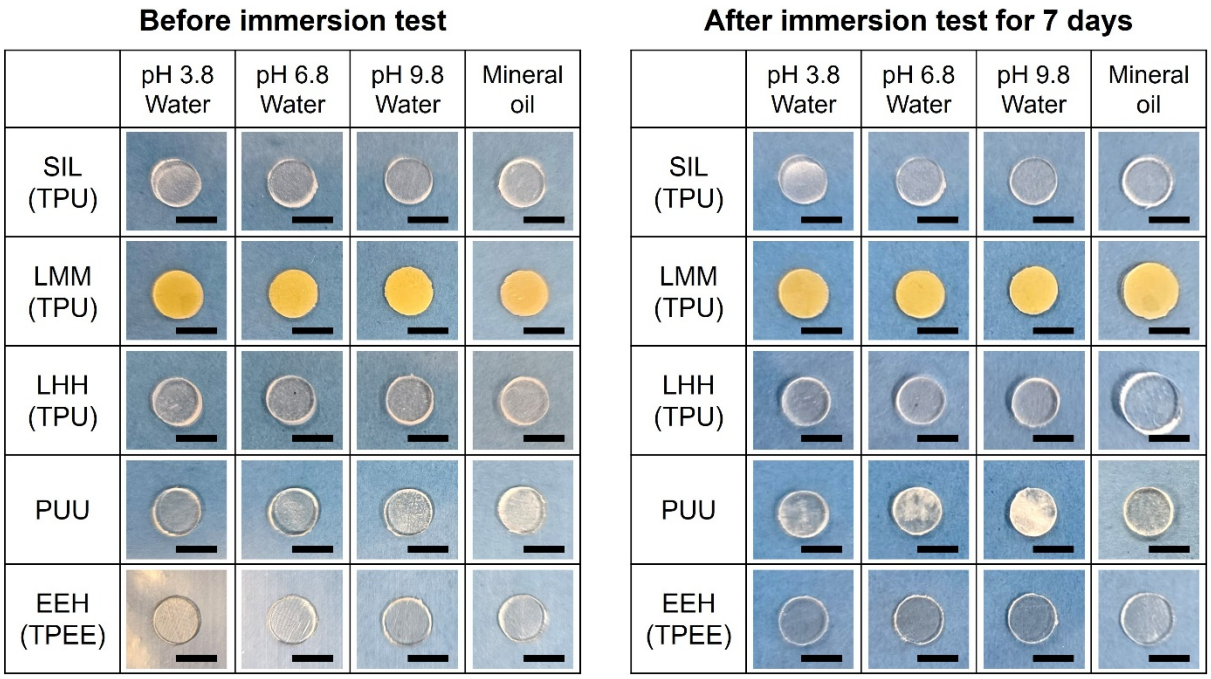

Fig. S12: Photographs showing ether-based thermoplastic elastomers before and after the chemical stability tests by immersion. Scale bars: 5 mm.

Notes: Unless specified below, all the TPUs show no damages or changes on material surfaces and integrity after testing. LMM and LHH TPUs swell in mineral oil after testing. PUU shows a degree of surface damage when exposed to pH 6.8 and 9.8 water. EEH shows no changes during the test period except for a small degree of swelling in mineral oil.

Table S4: Chemical stability results of the selected ether-based thermoplastic elastomers by immersion tests.

Test liquid	Time / day	Weight change in the biobased elastomers / %				
		SIL (TPU)	LMM (TPU)	LHH (TPU)	PUU	EEH (TPEE)
pH 3.8	1	–0.76 ± 0.62	0.61 ± 0.45	0.48 ± 0.17	–0.36 ± 0.60	0.86 ± 0.76
Water	7	–0.76 ± 1.07	0.61 ± 0.45	–0.12 ± 0.45	0.00 ± 0.90	0.86 ± 0.17
pH 6.8	1	0.74 ± 0.61	–0.50 ± 0.35	–0.12 ± 0.47	0.51 ± 0.64	0.62 ± 0.87
Water	7	0.99 ± 0.35	–0.75 ± 0.62	0.38 ± 1.41	0.89 ± 0.79	0.86 ± 0.76
pH 9.8	1	0.52 ± 0.37	0.75 ± 0.61	–0.73 ± 0.30	0.14 ± 0.99	0.00 ± 0.62
Water	7	0.78 ± 0.63	0.76 ± 0.63	–0.73 ± 1.37	0.27 ± 1.71	0.76 ± 0.63
Mineral	1	3.02 ± 0.32	56.82 ± 0.35	41.83 ± 0.26	3.87 ± 0.48	9.95 ± 1.67
oil	7	5.28 ± 0.29	59.09 ± 0.37	84.98 ± 0.83	9.35 ± 0.63	30.07 ± 0.53

Table S5: Thermal transition temperatures of ether-based TPUs measured by DSC. Glass transition temperature midpoints are reported.

Sample code	*T_g / °C	**T_m / °C
SIL	–38.5	86.6
SIM	–37.5	99.7
SML	–33.8	130.6
SMM	–32.9	134.0
SHL	–38.7	115.5
SHM	–38.2	119.0
LIM	–51.0	126.7
LIH	–51.0	129.1
LMM	–50.6	134.5
LMH	–50.1	141.4
LHM	–51.4	126.7
LHH	–51.0	134.7

*T_g: Glass transition temperature; **T_m: Melting point

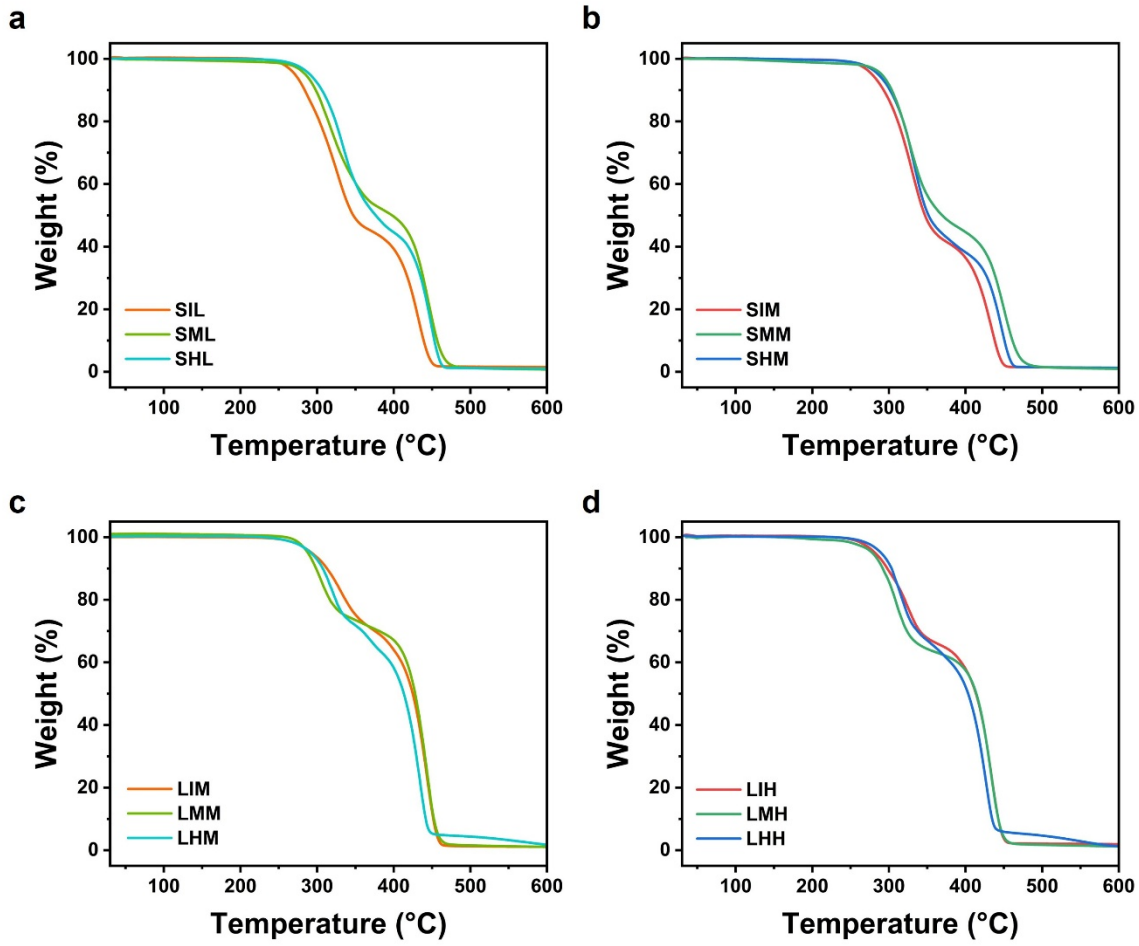

Fig. S13: TGA graphs of ether-based TPU elastomers.

Table S6: Thermal degradation onset temperatures and weight losses of biobased TPUs by TGA.

Sample code	T_{d1}^{onset} / °C	ΔW_{d1} / %	T_{d2}^{onset} / °C	ΔW_{d2} / %
SIL	266.5	55.3	402.3	39.7
SIM	280.7	57.5	410.8	37.3
SML	290.0	48.9	424.7	46.5
SMM	294.6	51.7	428.4	43.7
SHL	295.5	51.2	426.5	45.0
SHM	293.5	58.4	428.0	37.4
LIM	295.9	28.9	413.1	66.3
LIH	274.7	35.5	407.0	58.4
LMM	278.2	31.5	411.1	64.9
LMH	284.3	36.7	411.1	56.8
LHM	294.3	32.5	410.7	62.0
LHH	290.3	36.0	400.2	59.8

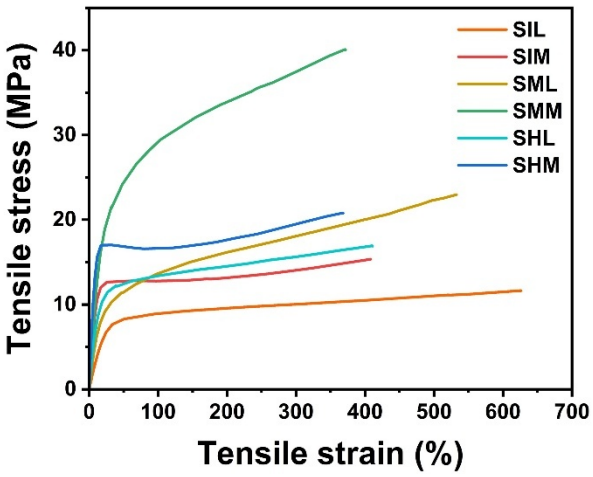

Fig. S14: Representative tensile stress-strain curves of the ether-based TPUs with the short polyether diol (synthesis time: 7 h).

Table S7: Summary of tensile properties and hardness values of the ether-based TPUs prepared with the short polyether diol (synthesis time: 7 h).

Sample code	Tensile stress at 15% strain / MPa	Tensile strength / MPa	Elongation at break / %	Shore D hardness
SIL	4.80 ± 0.89	10.94 ± 0.74	590 ± 113	38.3 ± 1.7
SIM	13.01 ± 1.11	15.25 ± 0.36	395 ± 18	55.3 ± 0.9
SML	6.81 ± 1.15	22.06 ± 1.27	508 ± 40	53.0 ± 1.4
SMM	13.90 ± 1.26	37.47 ± 1.72	358 ± 51	59.7 ± 1.2
SHL	10.10 ± 1.12	19.75 ± 2.63	466 ± 51	57.7 ± 1.7
SHM	16.67 ± 1.15	20.36 ± 1.30	337 ± 39	67.3 ± 1.7

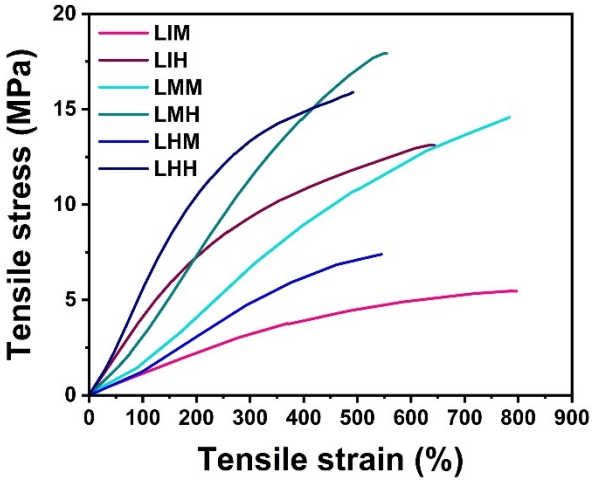

Fig. S15: Representative tensile stress-strain curves of the ether-based TPUs with the long polyether diol (synthesis time: 19 h).

Table S8: Summary of tensile properties and hardness values of the ether-based TPUs prepared with the longer polyether diol (synthesis time: 19 h).

Sample code	Tensile stress at 15% strain / MPa	Tensile strength / MPa	Elongation at break / %	Shore A hardness
LIM	0.19 ± 0.02	5.68 ± 0.28	791 ± 23	50.7 ± 1.2
LIH	0.68 ± 0.10	12.51 ± 0.73	651 ± 30	81.0 ± 1.4
LMM	0.22 ± 0.06	13.18 ± 1.17	771 ± 30	69.0 ± 2.4
LMH	0.41 ± 0.03	13.72 ± 1.82	606 ± 72	70.7 ± 1.7
LHM	0.19 ± 0.03	8.00 ± 0.80	527 ± 12	66.7 ± 1.2
LHH	0.54 ± 0.06	16.65 ± 0.82	520 ± 23	75.7 ± 2.9

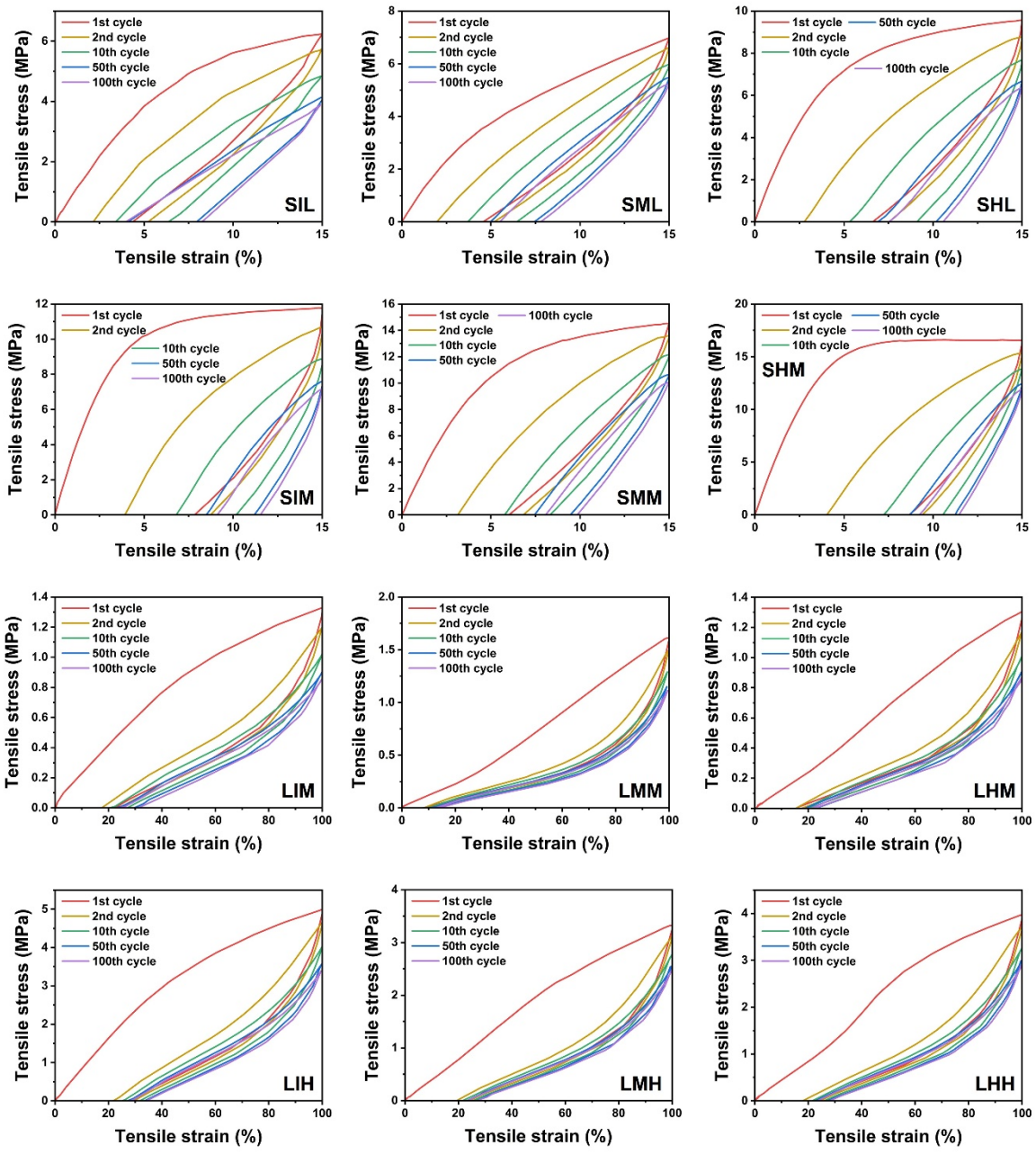

Fig. S16: Cyclic tensile test curves of ether-based TPUs.

Table S9: Hysteresis ratios at the 10th and 100th cycles, as well as the residual strain measured from the cyclic tensile tests on ether-based TPUs.

Sample code	Hysteresis ratio at the 10th cycle, h_{10th}	Hysteresis ratio at the 100th cycle, h_{100th}	Residual strain after 100 cycles / %
SIL	0.604	0.505	8.06
SIM	0.931	0.560	11.53
SML	0.540	0.407	7.80
SMM	0.693	0.511	9.87
SHL	0.802	0.763	10.55
SHM	0.723	0.507	11.40
LIM	0.219	0.196	29.28
LIH	0.253	0.234	32.55
LMM	0.154	0.125	12.39
LMH	0.186	0.163	26.63
LHM	0.141	0.116	22.56
LHH	0.222	0.208	27.94

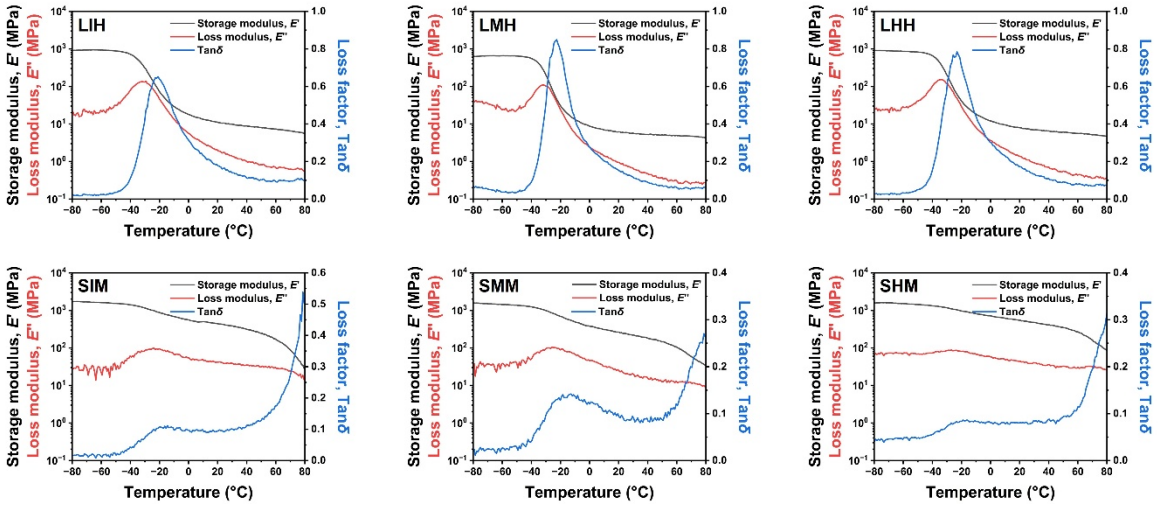

Fig. S17: DMA graphs of selected ether-based TPUs.

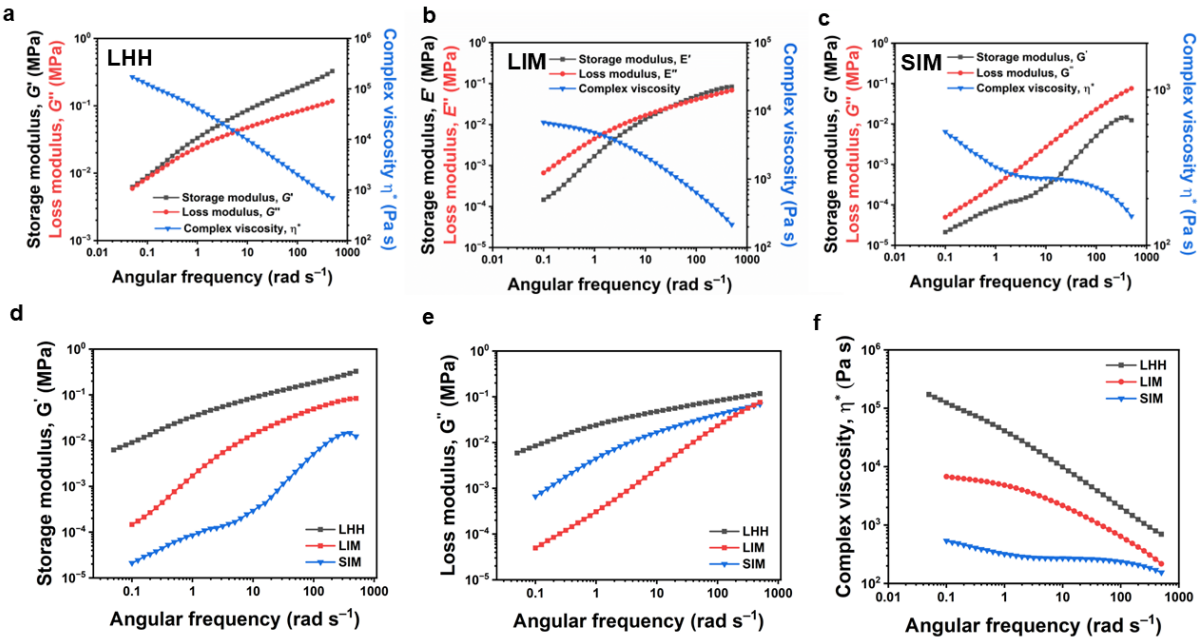

Fig. S18: Rheological graphs of selected ether-based TPUs showing (a-c) individual rheological properties: LHH, LIM and SIM, as well as (d-f) their comparisons.

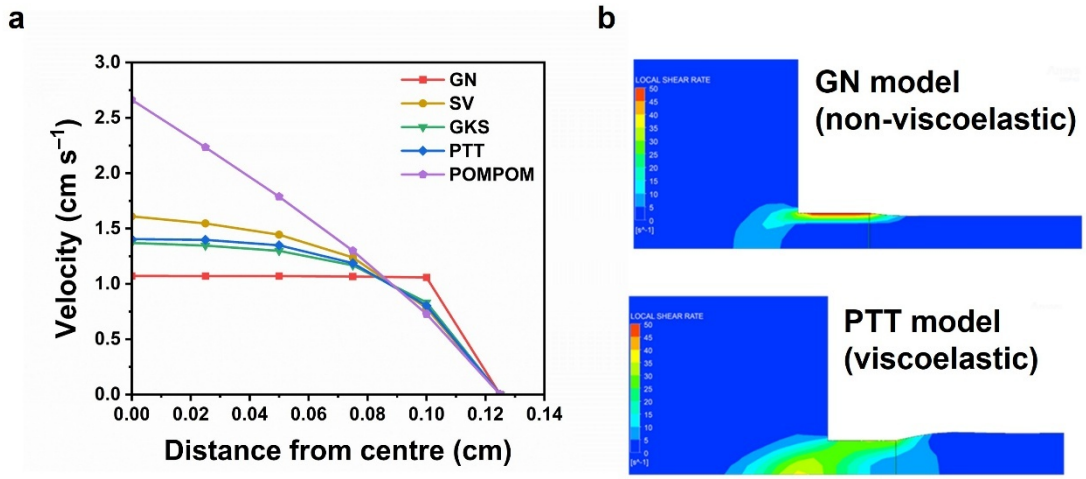

Fig. S19: A comparison of the mathematical models for the die swell of LHH. Simulation with the Generalised Newtonian (GN), simplified viscoelastic (SV), Giesekus (GSK), Phan-Thien Tanner (PTT) and Pom-Pom (POMPOM). **a**, velocity gradients at different positions within the extrusion die for LHH. **b**, a comparison of non-viscoelastic GN model and viscoelastic PTT model.

Notes: Simulations of the TPU being extruded through a die clearly show the plug effect as the polymer moves from the reservoir into the die, and an increase in diameter caused by die swelling.

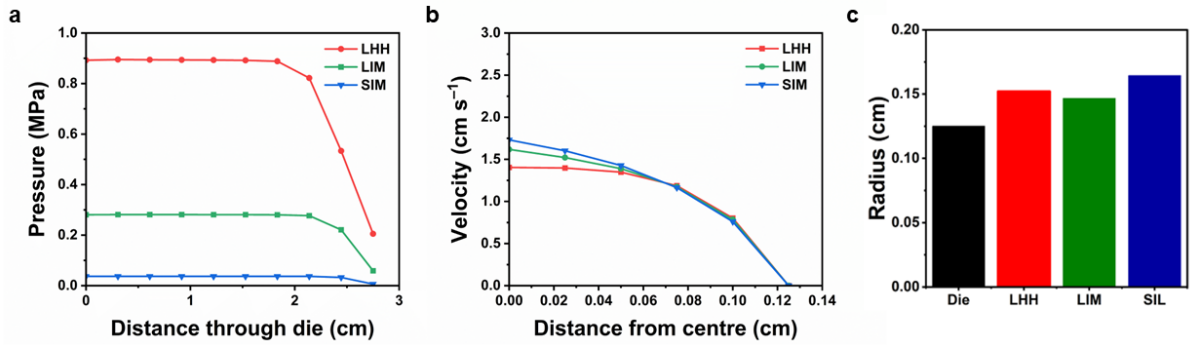

Fig. S20: Extrusion simulation using PTT model comparing different ether-based TPUs. **a**, pressure drop, **b**, velocity gradients and **c**, increase of radius due to die swell of LHH, LIM and SIM simulated with the PTT model.

Table S10: The MFI of selected ether-based TPUs.

Sample code	MFI / g 10 min^{-1}
SIM	18.9 ± 0.7
SMM	6.0 ± 0.2
SHM	10.9 ± 0.7
LIH	13.9 ± 0.9
LMH	8.6 ± 0.7
LHH	11.9 ± 0.1

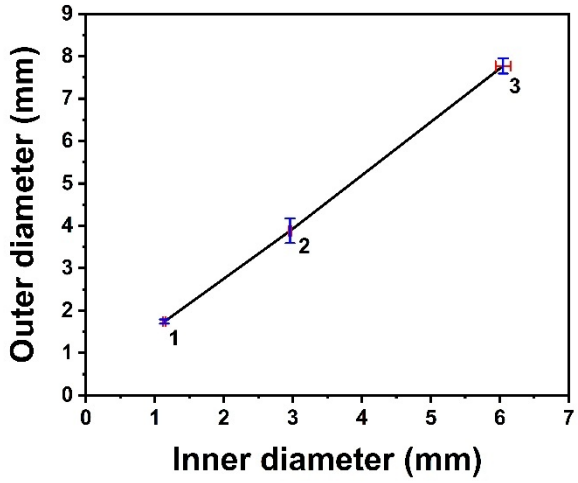

Fig. S21: The inner and outer diameters of the TPU (LIH) elastomer tubings. Red and blue error bars indicate the standard deviations in inner and outer diameters, respectively.

Table S11: The inner and outer diameters of the extruded TPU (LIH) tubings.

Tube	Inner diameter / mm	Outer diameter / mm	Wall thickness / mm
1	1.14 ± 0.02	1.74 ± 0.05	0.30 ± 0.03
2	2.96 ± 0.02	3.88 ± 0.29	0.46 ± 0.01
3	6.05 ± 0.11	7.77 ± 0.18	0.86 ± 0.02

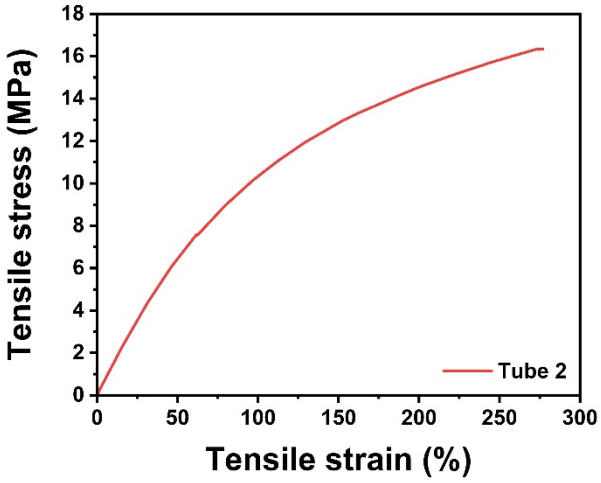

Fig. S22: Representative tensile stress-strain curve of the TPU (LIH) tubing.

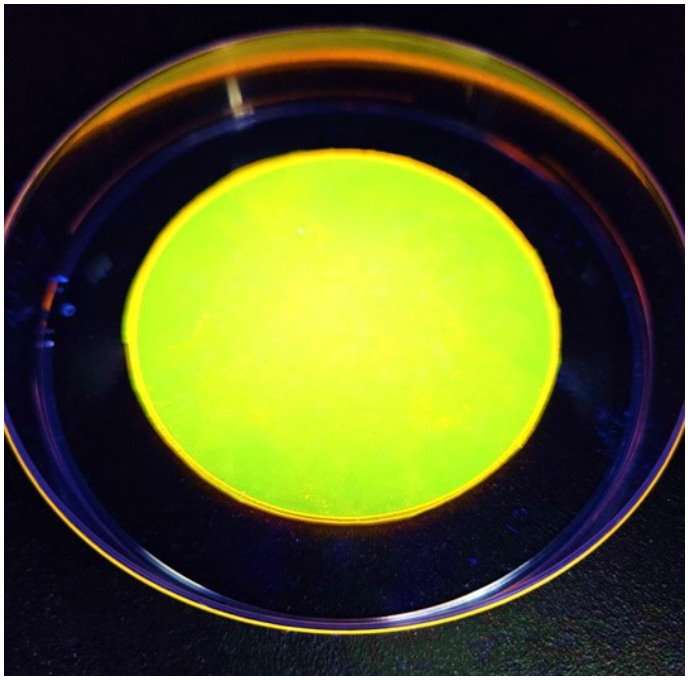

Fig. S23: Fluorescence of curcumin-dyed ether-based TPU (LHH) under a UV light.

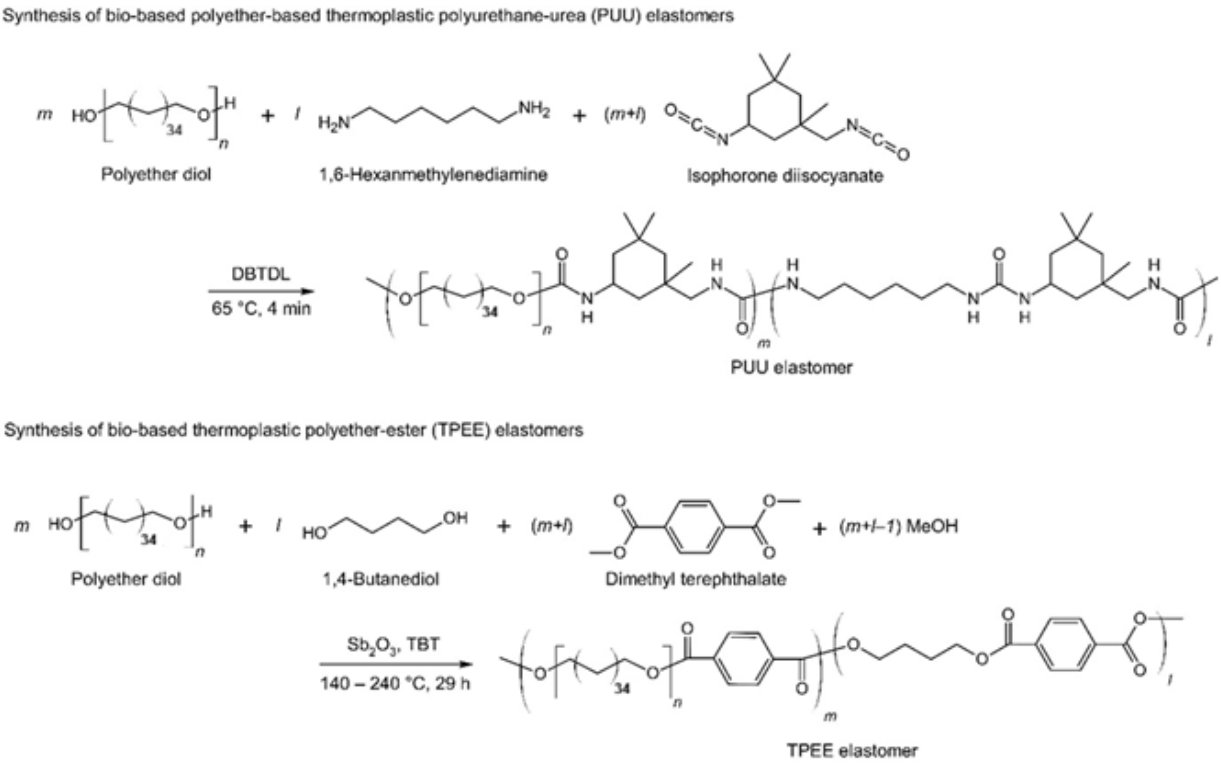

Fig. S24: Chemical scheme showing synthesis of ether-based PUU and TPEE elastomers.

Table S12: Summary of ether-based PUU and TPEE elastomer formulations.

Polyether diol synthesis time / h	Hard segment		Molar ratio (Polyether diol:chain extender: diiocyanate)	Hard segment content / % w/w	Soft segment content / % w/w	Sample code
	Chain extender	Diisocyanate or DMT				
7	HMDA	IPDI	1:1.67:3.50	31	69	PUU
7	BDO	DMT	1:0.28:1.16	12.2	87.8	EEL
7	BDO	DMT	1:3.90:4.45	39.3	60.7	EEH

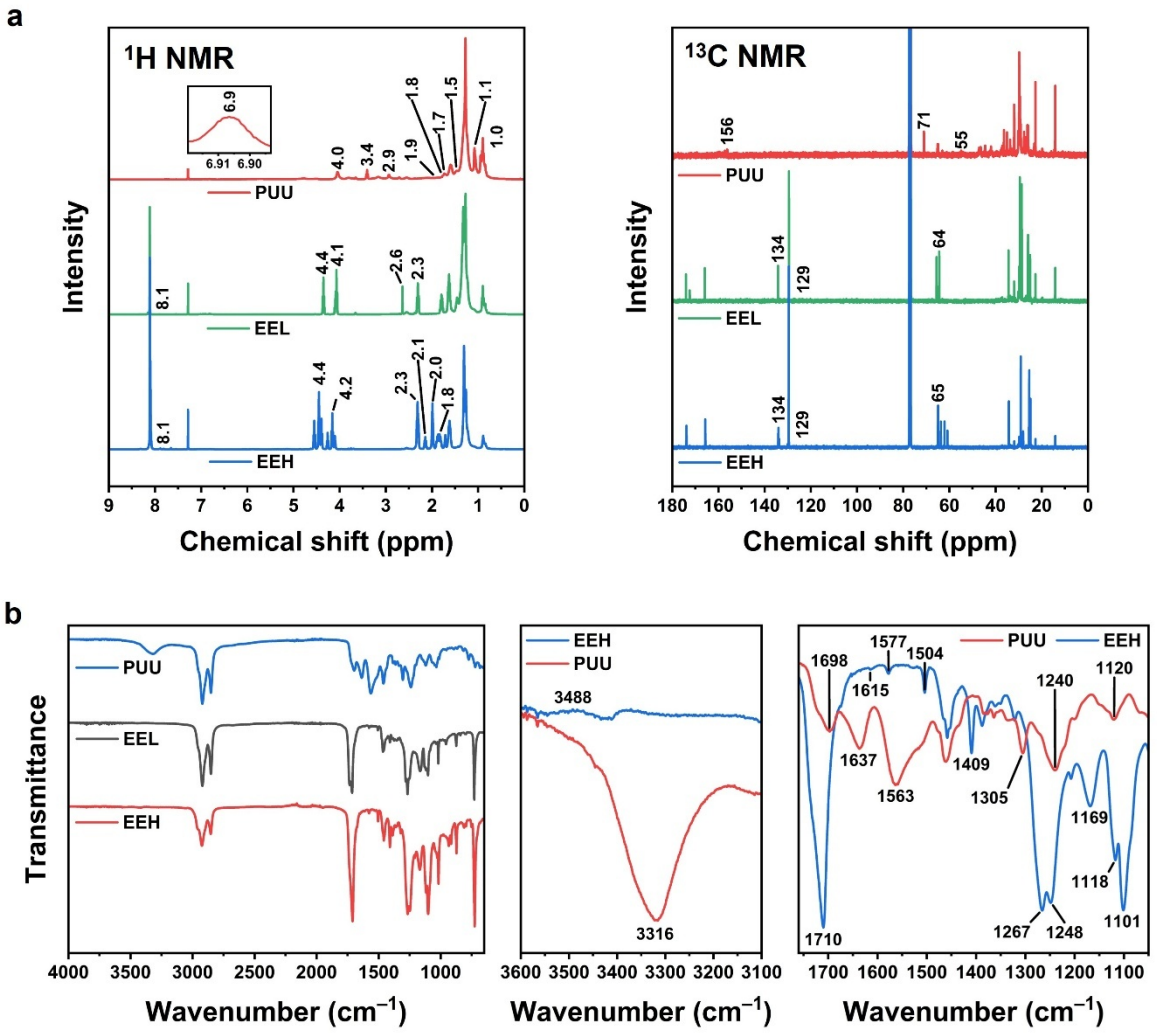

Fig. S25: NMR and FTIR spectra of ether-based PUU and TPEE elastomers. a, ^{1}H and ^{13}C NMR spectra of PUU and TPEEs. The spectra were moved vertically for visual clarity. **b**, FTIR spectra of PUU and TPEEs.

Notes: PUU shows N–H proton peak at 6.9 ppm from the presence of two N–H groups in urea linkages which are able to form bidentate hydrogen bonding.[93] Cycloaliphatic and aliphatic group protons are shown between 1.0 and 2.0 ppm for PUU due to the use of IPDI.[15] A distinct IPDI methylene proton peak from PUU is also shown at 2.9 ppm.[21,22] The CH_2–O and CH_2–N protons are shown at 3.4 ppm and 4.0 ppm for PUU. The CH_2–O proton peaks for EEL and EEH TPEE are shown between 4.1 ppm and 4.4 ppm, which deshield and shift. A singlet aromatic proton peak is observed at 8.1 ppm inherited from DMT in TPEE hard segment

structure.[94] Under ^{13}C NMR, the peak at 156 ppm is related to the carbonyl (C=O) group in the urea linkages, whereas EEL and EEH TPEE show peaks between 174 ppm and 166 ppm for the carbonyls from the carboxylic end group, as well as adjacent to the polyether diol and BDO chain extender, respectively.[23] EEL and EEH TPEE show aromatic ring carbons from DMT at 134 ppm and 129 ppm.[84] The peaks at 71, 65 or 64 ppm are attributed to the O-bonded carbon (O–CH_2).[21,84] PUU shows the N-bonded carbon (N–CH_2) at 55 ppm.[85] The peaks under 40 ppm are correlated with the carbon backbone structure of the elastomers.[21,78]

The FTIR spectra of PUU elastomers show the broad peak at 3316 cm^{-1} which can be attributed to N–H stretching of amide A.[15] The urea related peaks are also shown at 3316 cm^{-1} (amide A, N–H stretching), 1637 cm^{-1} (amide I, C=O stretching), 1563 cm^{-1} and 1305 cm^{-1} (amide II, N–H bending and C–N stretching), 1240 cm^{-1} (amide III, N–H bending) and 1120 cm^{-1} (O–C–C stretching).[15,24,25] EEH TPEE elastomer shows ester-related peaks at 1710 cm^{-1} (C=O stretching), as well as peaks between 1267 and 1101 cm^{-1} (C–O stretching vibrations from ester and ether). Aromatic hard segment structure is also shown by the peaks at 1615 – 1504 cm^{-1} (aromatic C=C stretching) and 1409 cm^{-1} (aromatic C–H in plane vibration).[80,81]

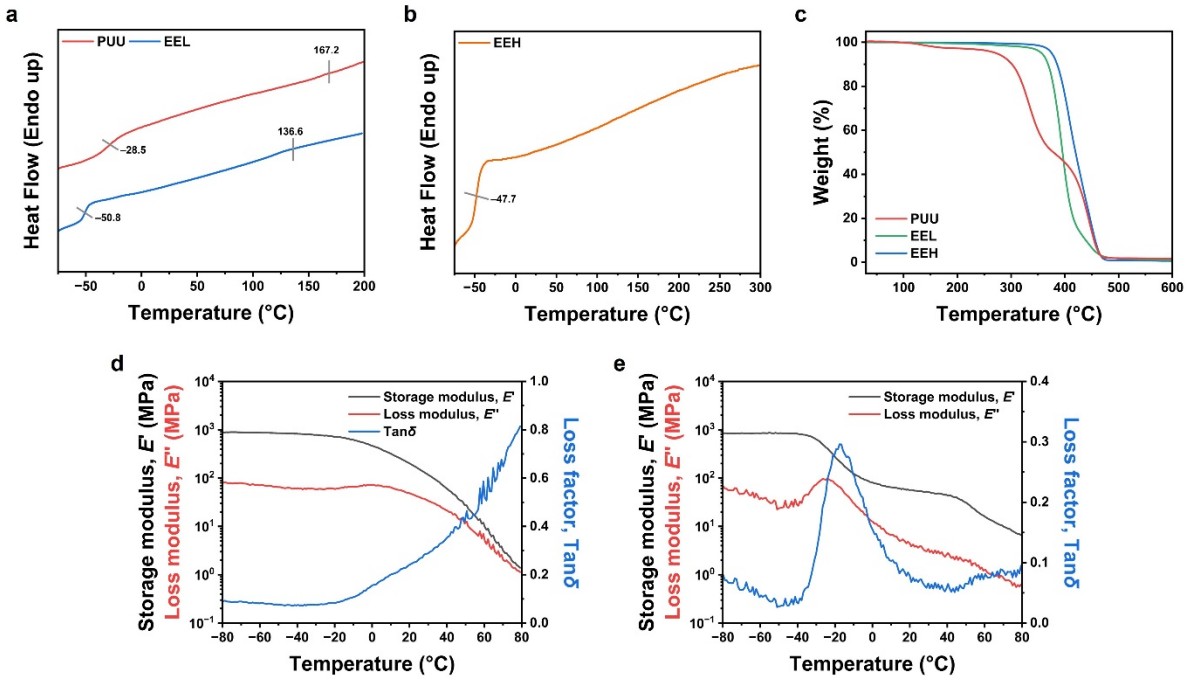

Fig. S26: DSC, TGA and DMA results of ether-based PUU and TPEE elastomers. a and **b,** DSC 2nd heating curves of PUU and TPEE (EEL and EEH). DSC curves were shifted vertically for visual clarity. **c**, TGA graph of PUU and TPEE (EEL and EEH). DMA curves of **d**, PUU and **e**, TPEE (EEH).

Notes: Both PUU and EEL show minor broad melting peaks, suggesting mostly amorphous with low crystallinity. PUU exhibits the highest melting point out of all the biobased elastomer formulations investigated in this work, mainly due to the bidentate hydrogen bonding sites discussed previously. In the TPEE, increasing the hard segment ratio diminishes the melting peak from EEL to EEH. It has been reported that with a higher hard segment, the crystallite size and crystalline structure of copolymers have more variations [23] causing a broader and more invisible melting peak.

Table S13: Thermal transition temperatures of ether-based PUU and TPEE elastomers measured by DSC. Glass transition temperature midpoints are reported.

Sample code	*T_g / °C	**T_m / °C
EEL	–50.8	136.6
EEH	–47.7	-
PUU	–28.5	167.2

Table S14: Thermal degradation onset temperatures and weight losses of ether-based PUU and TPEE elastomers by TGA.

Sample code	T_{d1}^{onset} / °C	ΔW_{d1} / %	T_{d2}^{onset} / °C	ΔW_{d2} / %
PUU	296.4	47.6	418.9	44.8
EEL	367.9	87.2	415.5	9.5
EEH	379.3	58.1	433.8	39.9

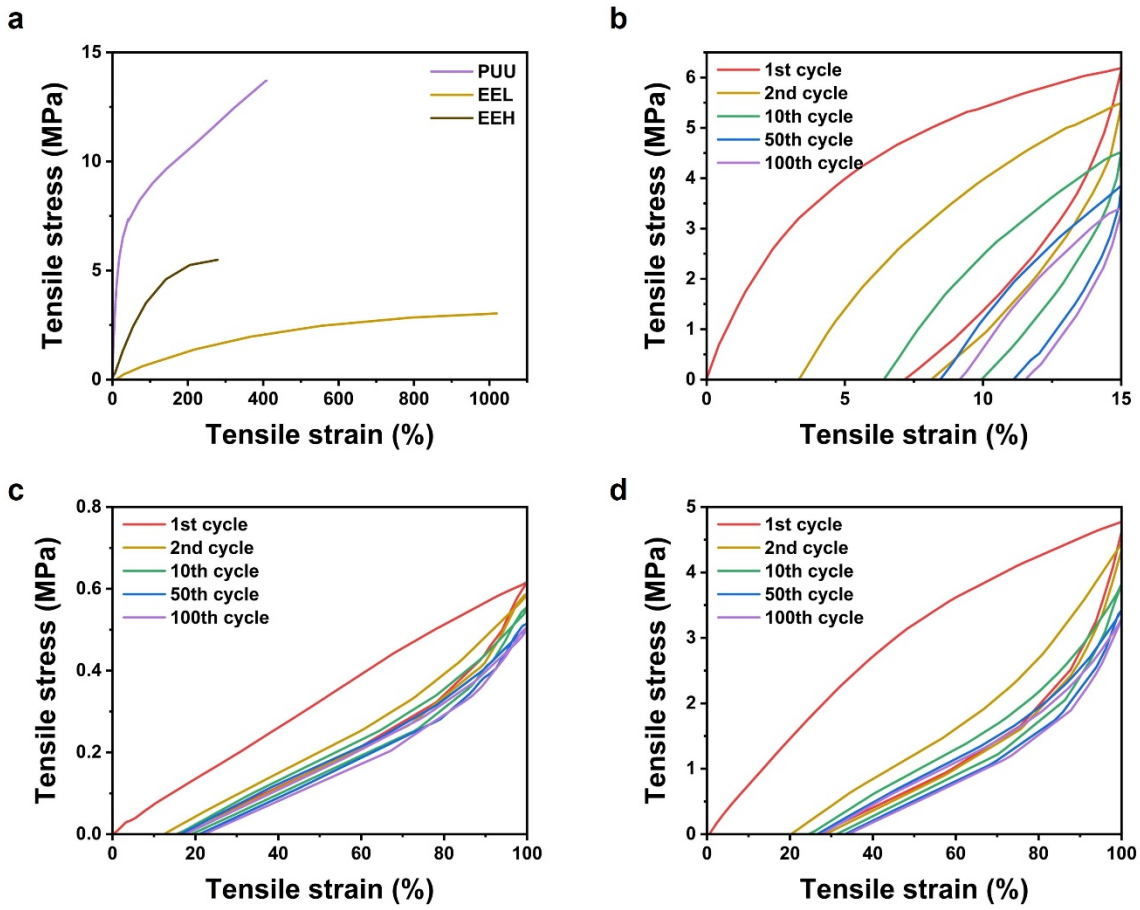

Fig. S27: Tensile and cyclic tensile stress-strain curves of ether-based PUU and TPEE elastomers. a, Representative tensile stress-strain curves. Cyclic tensile stress-strain curves of **b**, PUU, **c**, EEL (TPEE) and **d**, EEH (TPEE).

Table S15: Summary of tensile properties and hardness values of ether-based PUU and TPEEs.

Sample code	Tensile stress at 15% strain / MPa	Tensile strength / MPa	Elongation at break / %	Shore D hardness
PUU	5.19 ± 0.60	13.42 ± 0.66	376 ± 70	45.3 ± 3.9
EEL	0.09 ± 0.01	2.61 ± 0.23	995 ± 65	32.3 ± 1.2
EEH	0.82 ± 0.10	5.19 ± 0.26	268 ± 7	73.3 ± 3.7

Table S16: Hysteresis ratios at the 10th and 100th cycles, as well as the residual strain determined from the cyclic tensile tests on ether-based PUU and TPEEs.

Sample code	Hysteresis ratio at the 10th cycle, h_{10th}	Hysteresis ratio at the 100th cycle, h_{100th}	Residual strain after 100 cycles / %
PUU	0.838	0.700	11.46
EEL	0.158	0. 082	22.03
EEH	0.233	0.193	34.14

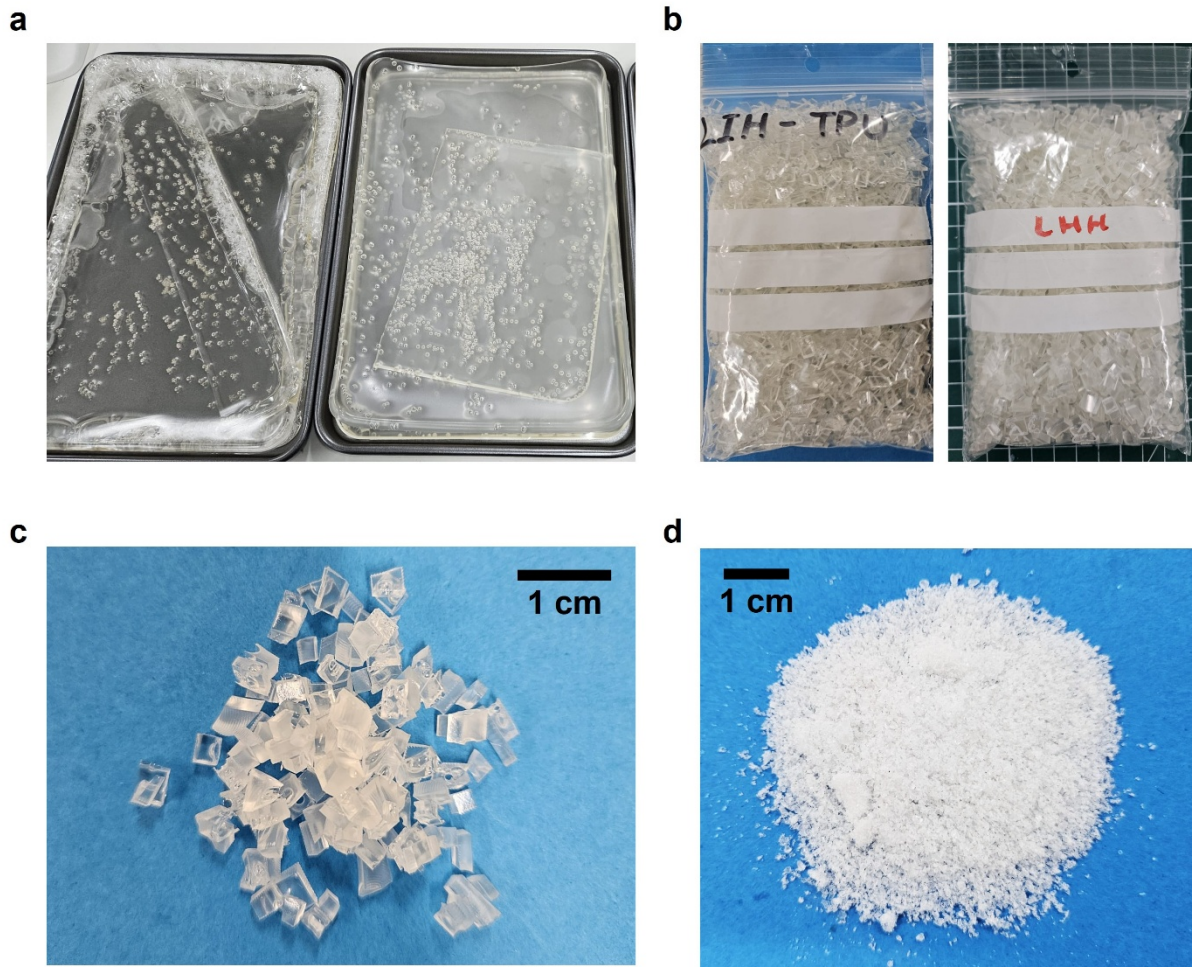

Fig. S28: Photographs showing bulk-produced renewable ether-based TPU elastomers. **a**, TPU elastomers as synthesised and collected on baking trays (left) LIH and (right) LHH (about 1.4 – 1.5 kg each). **b**, Shredded LIH (left) and LHH (right). **c**, A close look of LHH shreds. **d**, LHH powders by cryo-milling.

Table S17: The density of renewable ether-based elastomers in this study.

Sample code	Density, ρ / g cm^{-3}
SIL	0.94 ± 0.02
SIM	0.95 ± 0.02
SML	0.97 ± 0.02
SMM	0.98 ± 0.00
SHL	0.96 ± 0.01
SHM	0.97 ± 0.01
LIM	0.90 ± 0.06
LIH	0.92 ± 0.03
LMM	0.94 ± 0.03
LMH	0.96 ± 0.02
LHM	0.93 ± 0.02
LHH	0.95 ± 0.02
EEL	0.90 ± 0.02
EEH	0.99 ± 0.02
PUU	0.97 ± 0.01

References

15 T. Griggs, J. Ahmed, H. Majd, M. Edirisinghe, B. Chen. et al. A bio-based thermoplastic polyurethane with triple self-healing action for wearable technology and smart textiles. *Mater. Adv.* 2024, **5**, 6210–6221.

16 A. Sonseca, M. El Fray. Enzymatic synthesis of an electrospinnable poly(butylene succinate-co-dilinoleic succinate) thermoplastic elastomer. *RSC Adv.* 2017, **7**, 21258–21267.

21 A. Mouren, L. Avérous. Aromatic thermoplastic polyurethanes synthesized from different potential sustainable resources. *Eur. Polym. J.* 2023, **197**, 112338.

22 D. J. Harris, R. A. Assink, M. Celina. NMR analysis of oxidatively aged HTPB/IPDI polyurethane rubber: Degradation products, dynamics, and heterogeneity. *Macromolecules* 2001, **34**, 6695–6700.

23 A. Kumar, A. P. M. Kentgens. Unravelling crosslinking and molecular structure in complex polyurethanes via advanced multinuclear solid-state NMR. *Polymer (Guildf)* 2025, **325**, 128245.

24 B. C. Smith. Infrared Spectroscopy of Polymers, IX: Pendant Ester Polymers and Polycarbonates. *Spectroscopy* 2022, **37**, 16-19.

25 M. Gorbunova, D. V. Anokhin, A. Abukaev, D. Ivanov. Impact of Soft Segment Composition on Phase Separation and Crystallization of Multi-Block Thermoplastic Polyurethanes Based on Poly(butylene adipate) Diol and Polycaprolactone Diol. *Crystals (Basel)* 2023, **13**, 1447.

32 N. Wingborg. Increasing the tensile strength of HTPB with different isocyanates and chain extenders. *Polym Test* 2002, **21**, 283–287.

72. J. Ren, L. Zhu, X. Zhang, Y. Luo, X. Zhong, B. Li, Y. Wan, K. Zhang. Variation characteristics of acid rain in Zhuzhou, Central China over the period 2011-2020. *J. Environ. Sci.* 2024, **138**, 496–505.

73. J. Tarun, J. Susan, J. Suria, V.J. Susan, S. Criton. Evaluation of pH of bathing soaps and shampoos for skin and hair care. *Indian J. Dermatol.* 2014, **59**, 442–444.

74. K. R. Hinga, Effects of pH on coastal marine phytoplankton. *Marine Ecol. Prog. Ser.* 2002, **238**, 281–300.

75. R. Vaid, E. Yildirim, M.A. Pasquinelli, M.W. King. Hydrolytic degradation of polylactic acid fibers as a function of pH and exposure time. *Molecules* 2021, **26**, 7554.

76. C.N. Ward, P.E. LeBlanc, R.E. Burrell. Effects of composition and pH on the degradation of hyaluronate and carboxymethyl cellulose gels and release of nanocrystalline silver**.** *J. Appl. Biomater. Funct. Mater.* 2024, **22**, 22808000241257124.

77. N. Stachowiak. J. Kowalonek, j. Kozlowska, A. Burkowska-But. Stability studies, biodegradation tests, and mechanical properties of sodium alginate and Gellan gum beads containing surfactants. *Polymers* 2023, **15**, 2568.

78 S. R. K Chalasani, S. Dewasthale, E. Hablot, S. Shi. A Spectroscopic Method for Hydroxyl Value Determination of Polyols. *J. Am. Oil Chem. Soc.* 2013, **90**, 1787–1793.

79 M. Sokołowska, E. Stachowska, M. Czaplicka, M. El Fray. Effect of enzymatic versus titanium dioxide/silicon dioxide catalyst on crystal structure of ‘green’ poly[(butylene succinate)-co-(dilinoleic succinate)] copolymers. *Polym. Int.* 2021, **70**, 514–526.

80 J. Skrobot, W. Ignaczak, M. El Fray. Hydrolytic and enzymatic degradation of flexible polymer networks comprising fatty acid derivatives. *Polym. Degrad. Stab.* 2015, **120**, 368–376.

81 Y. Nurhamiyah, S. Yoon, B. Chen. Wholly Biobased Polyamide Thermoplastic Elastomer-Cellulose Nanocomposites. *Macromol. Mater. Eng.* 2022, **307**, 2200120.

82 N. S. Vrandečić, M. Erceg, M. Jakić, I. Klarić. Kinetic analysis of thermal degradation of poly(ethylene glycol) and poly(ethylene oxide)s of different molecular weight. *Thermochim. Acta* 2010, **498**, 71–80.

83 S. Yoon, B. Chen. Biomimetic Elastomer-Clay Nanocomposite Hydrogels with Control of Biological Chemicals for Soft Tissue Engineering and Wound Healing. *ACS Appl. Bio. Mater.* 2025, **8**, 2492–2505.

84 M. Alves. Carbon dioxide and vegetable oil for the synthesis of biobased polymer precursors. PhD thesis, Universit´e de Bordeaux 2016.

85 K. Schmidt-Rohr, J.-D. Mao, D.C. Olk, J. M. Bremner. Nitrogen-Bonded Aromatics in Soil Organic Matter and Their Implications for a Yield Decline in Intensive Rice Cropping. *PNAS* 2004, **101**, 6351–6354.

86 M. A. Gorbunova, E. V. Komov, L. Y. Grunin, M. S. Ivanova, A. F. Abukaev, A. M. Imamutdinova, D. A. Ivanov, D. V. Anokhin. The effect of separation of blocks on the crystallization kinetics and phase composition of poly(butylene adipate) in multi-block thermoplastic polyurethanes. *Phys. Chem. Chem. Phys.* 2022, **24**, 902–913.

87 P. X. Thinh, C. Basavaraja, D. G. Kim, D. S. Huh. Characterization and electrochemical behaviors of honeycomb-patterned poly(N-vinylcarbazole)/polystyrene composite films. *Polym. Bull.* 2012, **69**, 81–94.

88 B. B. Yilma, J. F. Luebben, G. Nalankilli. The Effect of Air, Ar and O2 Plasmas on the Electrical Resistivity and Hand-Feel Properties of Polyester/Cotton Blend Fabric. *Fibers* 2020, **8**, 17.

89 M. Reinecker, V. Soprunyuk, M. Fally, A. Sánchez-Ferrer, W. Schranz. Two glass transitions of polyurea networks: Effect of the segmental molecular weight. *Soft Matter* 2014, **10**, 5729–5738.

90 M. Nofar, E. Büşra Küçük, B. Batı. Effect of hard segment content on the microcellular foaming behavior of TPU using supercritical CO_2. *J. Supercrit. Fluids* 2019, **153**, 104590.

91 B. D. Akkoyun, A. A. Wis, R. Yıldırım, Ü. Makal, G. Özkoç, M. Kodal. Enhanced Crystallinity Through Melt Annealing of Thermoplastic Polyurethanes. *J. Appl. Polym. Sci.* 2024, **142**, e56593.

92 M. S. S. Sadeghian, A. Raisi. A thermodynamic study on relationship between gas separation properties and microstructure of polyurethane membranes. *Sci. Rep.* 2023, **13**, 6038.

93 T. L. Chantawansri, Y. R. Sliozberg, J. W. Andzelm, A. J. Hsieh. Coarse-grained modeling of model poly(urethane urea)s: Microstructure and interface aspects. *Polymer (Guildf)* 2012, **53**, 4512–4524.

94 A. Martínez De Ilarduya, S. Muñoz-Guerra. Chemical structure and microstructure of poly(alkylene terephthalate)s, their copolyesters, and their blends as studied by NMR. *Macromol. Chem. Phys.* 2014, **215**, 2138–2160.